

Strong Correlations and Orbital Texture in Single-Layer 1T-TaSe₂

Yi Chen^{1,2,†}, Wei Ruan^{1,2,†}, Meng Wu^{1,2,†}, Shujie Tang^{3,4,5,6,7,†}, Hyejin Ryu^{5,8}, Hsin-Zon Tsai^{1,9},
Ryan Lee¹, Salman Kahn¹, Franklin Liou¹, Caihong Jia^{1,2,10}, Oliver R. Albertini¹¹, Hongyu
Xiong^{3,4}, Tao Jia^{3,4}, Zhi Liu⁶, Jonathan A. Sobota^{3,5}, Amy Y. Liu¹¹, Joel E. Moore^{1,2}, Zhi-Xun
Shen^{3,4}, Steven G. Louie^{1,2}, Sung-Kwan Mo⁵, and Michael F. Crommie^{1,2,12,*}

¹*Department of Physics, University of California, Berkeley, CA 94720, USA*

²*Materials Sciences Division, Lawrence Berkeley National Laboratory, Berkeley, California 94720, USA*

³*Stanford Institute for Materials and Energy Sciences, SLAC National Accelerator Laboratory and Stanford University, Menlo Park, CA 94025, USA*

⁴*Geballe Laboratory for Advanced Materials, Departments of Physics and Applied Physics, Stanford University, Stanford, CA 94305, USA*

⁵*Advanced Light Source, Lawrence Berkeley National Laboratory, Berkeley, CA 94720, USA*

⁶*CAS Center for Excellence in Superconducting Electronics, Shanghai Institute of Microsystem and Information Technology, Chinese Academy of Sciences, Shanghai 200050, China*

⁷*School of Physical Science and Technology, Shanghai Tech University, Shanghai 200031, China*

⁸*Center for Spintronics, Korea Institute of Science and Technology, Seoul 02792, South Korea*

⁹*International Collaborative Laboratory of 2D Materials for Optoelectronic Science & Technology of Ministry of Education, Engineering Technology Research Center for 2D Material Information Function Devices and Systems of Guangdong Province, Shenzhen University, Shenzhen 518060, China*

¹⁰*Henan Key Laboratory of Photovoltaic Materials and Laboratory of Low-dimensional Materials Science, School of Physics and Electronics, Henan University, Kaifeng 475004, China*

¹¹*Department of Physics, Georgetown University, Washington, DC 20057, USA*

¹²*Kavli Energy Nano Sciences Institute at the University of California Berkeley and the Lawrence Berkeley National Laboratory, Berkeley, California 94720, USA*

30 † *These authors contributed equally to this work.*

31 **e-mail: crommie@berkeley.edu*

32

33 **Abstract:**

34 Strong electron correlation can induce Mott insulating behavior and produce intriguing states of
35 matter such as unconventional superconductivity and quantum spin liquids. Recent advances in
36 van der Waals material synthesis enable the exploration of Mott systems in the two-dimensional
37 limit. Here we report characterization of the local electronic properties of single- and few-layer
38 1T-TaSe₂ via spatial- and momentum-resolved spectroscopy involving scanning tunneling
39 microscopy and angle-resolved photoemission. Our results indicate that electron correlation
40 induces a robust Mott insulator state in single-layer 1T-TaSe₂ that is accompanied by unusual
41 orbital texture. Interlayer coupling weakens the insulating phase, as shown by reduction of the
42 energy gap and quenching of the correlation-driven orbital texture in bilayer and trilayer 1T-
43 TaSe₂. This establishes single-layer 1T-TaSe₂ as a useful platform for investigating strong
44 correlation physics in two dimensions.

45

46 Two-dimensional (2D) Mott insulators emerge when the Coulomb interaction (U) exceeds
47 the bandwidth (W) in partially-filled band systems that can be described by 2D Hubbard-like
48 models¹. Correlated electronic behavior in quasi-2D Mott insulators leads to collective quantum
49 phenomena^{2,3} such as high-temperature superconductivity which is widely believed to arise
50 through doping of Mott insulating copper-oxygen layers^{4,5}. Certain stacked graphene systems
51 have also recently been found to exhibit Mott-like insulating behavior and unconventional
52 superconductivity upon gating⁶⁻⁹. Layered transition metal dichalcogenides (TMDs) offer another
53 family of correlated quasi-2D materials, two examples being bulk 1T-TaS₂ and the surface of
54 bulk 1T-TaSe₂ which have long been known to host unusual insulating phases in the star-of-
55 David charge density wave (CDW) state¹⁰⁻¹³. Although widely believed to be Mott
56 insulators^{11,14,15}, the insulating nature of these bulk systems is complicated by interlayer CDW
57 stacking whose effects on the insulating phase remain controversial¹⁶. Interlayer hopping (which
58 increases W) and interlayer dielectric screening (which decreases U) are expected to suppress
59 Mott insulating behavior^{1,17,18}, but orbital stacking has also been predicted to open a
60 hybridization gap even in the absence of electron correlation^{16,19,20}.

61 Atomically-thin 1T-TMDs offer an ideal platform to differentiate the contributions of
62 electron correlation and interlayer effects in quasi-2D materials since single-layer systems can be
63 fully characterized in the absence of interlayer coupling. Without interlayer coupling the reduced
64 screening environment of a single-layer leads to increased Coulomb interaction and potentially
65 enhanced correlation phenomena²¹⁻²⁵. The effects of interlayer coupling can then be
66 systematically determined by adding new layers to a material one at a time and mapping out the
67 resulting stacking order and wavefunction properties. Previous studies on single-layer 1T-NbSe₂
68 and 1T-TaSe₂ have found unusual insulating behavior^{26,27}, but electronic wavefunction texture

69 and interlayer coupling effects were not examined. The nature of the insulating phase in these
70 single-layer materials thus remains inconclusive.

71 Here we report a combined scanning tunneling microscopy/spectroscopy (STM/STS), angle-
72 resolved photoemission spectroscopy (ARPES), and theoretical study of the electronic structure
73 of single-layer 1T-TaSe₂. Our results show that in the absence of interlayer coupling single-layer
74 1T-TaSe₂ hosts a Mott-insulating ground state that exhibits a 109 ± 18 meV energy gap and
75 unusual orbital texture. Bilayer and trilayer 1T-TaSe₂ with shifted stacking order exhibit
76 successively smaller energy gaps and show no signs of the unusual orbital texture seen in the
77 single-layer limit. The single-layer band structure and density of states of 1T-TaSe₂ are found to
78 be consistent with DFT+U calculations, confirming its Mott insulator nature. The unusual single-
79 layer orbital texture, however, is not captured by DFT+U, but is consistent with the behavior
80 expected for a weakly screened, strongly correlated 2D insulator. Reduction of the 1T-TaSe₂
81 bandgap and quenching of the unusual orbital texture by the addition of new layers shows that
82 the effect of interlayer coupling on shifted-stacked 1T-TaSe₂ is to weaken the Mott behavior.
83 The single-layer limit of 1T-TaSe₂ is thus unique in that strong correlation effects here are most
84 pronounced, affecting both the energy gap and electron wavefunction symmetry.

85 **Electronic structure of single-layer 1T-TaSe₂ in the CDW phase**

86 Our experiments were carried out on 1T-TaSe₂ thin films grown by molecular beam epitaxy
87 on epitaxial bilayer-graphene-terminated (BLG) 6H-SiC(0001), as sketched in Fig. 1a. The
88 crystal structure of 1T-TaSe₂ consists of a layer of Ta atoms sandwiched between two layers of
89 Se atoms in an octahedral coordination. Fig. 1b illustrates the hexagonal morphology of our 1T-
90 TaSe₂ islands, indicating high epitaxial growth quality. A triangular CDW superlattice is
91 observed on single-layer, bilayer, and trilayer 1T-TaSe₂, as seen in Figs. 1b, c, and

92 Supplementary Fig. 1 where each bright spot corresponds to a star-of-David CDW supercell.
93 Fourier analysis of STM images (Supplementary Fig. 2) together with low-energy electron
94 diffraction patterns (Supplementary Fig. 3) confirm the formation of a $\sqrt{13} \times \sqrt{13}$ CDW in
95 single-layer 1T-TaSe₂, similar to the commensurate CDW phase of bulk 1T-TaSe₂ at $T < 473$ K²⁸
96 (the atomic lattice and CDW superlattice are observed to have a relative rotation angle of
97 $\sim 13.9^\circ$). Reflection high-energy electron diffraction patterns (Fig. 1e) and X-ray photoelectron
98 spectroscopy (Fig. 1f) show the structural and chemical integrity of our single-layer 1T-TaSe₂
99 samples (1T and 1H islands do coexist in our samples due to the metastability of 1T-TaSe₂
100 (Supplementary Fig. 4)).

101 We experimentally determined the electronic structure of single-layer 1T-TaSe₂ in the star-
102 of-David CDW phase using ARPES and STS. Figs. 2a and 2b show the ARPES spectra of
103 single-layer 1T-TaSe₂ for *p*- and *s*-polarized light, respectively, obtained at $T = 12$ K. At low
104 binding energies the single-layer 1T-TaSe₂ ARPES spectra show strongly diminished intensity at
105 all observed momenta, indicating insulating behavior (some ARPES intensity from coexisting
106 1H-TaSe₂ islands can be seen crossing E_F at $k \approx 0.5 \text{ \AA}^{-1}$ (white dashed lines)²⁹). The CDW
107 superlattice potential induces band folding into a smaller CDW Brillouin zone (Fig. 2b inset).
108 One such band can be seen in the ARPES spectrum for *p*-polarized light (Fig. 2a) which shows a
109 prominent flat band centered at $E - E_F \approx -0.26$ eV within the first CDW Brillouin zone (black
110 dashed box). A more dispersive band can be resolved outside of the first CDW Brillouin zone
111 boundary (vertical dashed lines labeled A and B mark this boundary). These features have no
112 obvious photon-energy dependence (Supplementary Fig. 5) and are similar to bands observed by
113 ARPES at the surface of bulk samples of 1T-TaS₂^{16,30} and 1T-TaSe₂¹². For *s*-polarized light (Fig.

114 2b) the flat band is much less visible and a manifold of highly dispersive bands near the Γ -point
115 dominates the spectrum.

116 Our STM dI/dV spectrum (Fig. 3a (black curve)) confirms the insulating nature of single-
117 layer 1T-TaSe₂. The electronic local density of states (LDOS) reflected in dI/dV exhibits a
118 pronounced valence band peak at $V = -0.33$ V (labeled V_1) while dropping steeply at higher
119 energy until reaching zero at $V \approx -0.05$ V. The zero LDOS region bracketing the Fermi level
120 yields an energy gap of magnitude 109 ± 18 meV (see Supplementary Fig. 6 for gap
121 determination). The experimental LDOS does not rise again until a narrow conduction band peak
122 is observed centered at $V = 0.20$ V (labeled C_1) in the empty state regime. The LDOS drops to
123 zero again above the C_1 peak until higher-lying conduction band features are seen to rise at $V >$
124 0.45 V (e.g., C_2, C_3). Aside from spatial variation in the relative peak heights, this gapped
125 electronic structure is observed uniformly over the entire single-layer 1T-TaSe₂ surface
126 (Supplementary Fig. 7). No significant band-bending effects are observed for different tip-
127 sample separations (Supplementary Note 1 and Supplementary Figs. 8, 9). To test substrate
128 effects we also grew single-layer 1T-TaSe₂ on cleaved graphite (HOPG), which shows similar
129 STM spectra compared to single-layer 1T-TaSe₂/BLG (Supplementary Note 2 and
130 Supplementary Fig. 10). This indicates that the small increase in screening provided by HOPG²¹
131 (as shown by the slight downshift/upshift of empty-state/filled-state features in Supplementary
132 Fig. 10) does not significantly change the 1T-TaSe₂ behavior. We are so far unable to
133 experimentally test the effect of reducing screening below the level provided by BLG.

134 **Experimental orbital texture of single-layer 1T-TaSe₂**

135 To gain additional insight into the insulating ground state of single-layer 1T-TaSe₂, we
136 performed dI/dV spatial mapping of its energy-dependent orbital texture at constant tip-sample

137 separation (Figs. 3b-h). dI/dV maps measured at negative biases all display a similar pattern
138 where high-intensity LDOS is concentrated near the center of each star-of-David (Figs. 3b, c,
139 and Supplementary Fig. 11). The experimental empty-state LDOS of single-layer 1T-TaSe₂,
140 however, exhibits a completely different orbital texture. This is most clearly seen in the dI/dV
141 map taken at the lowest conduction band peak C_1 (Fig. 3d) where the center of each CDW
142 supercell is observed to be dark (i.e., no LDOS intensity). At this energy the LDOS exhibits an
143 unusual, interlocked “flower” pattern (circled by yellow dashed lines) consisting of six well-
144 defined “petals” (i.e., bright spots) located around the outer rim of each star-of-David. This
145 appearance is completely different from previous reports of conduction band LDOS in bulk 1T-
146 TaSe₂ and 1T-TaS₂^{13,31} (which show LDOS concentrated in the star-of-David centers), and is
147 clearly not due to defects since it follows the CDW periodicity. The 6-fold petal structure has a
148 different symmetry than the 3-fold arrangement of top-layer Se atoms in the spaces between each
149 star-of-David, but it shares the 6-fold symmetry of the Ta atom arrangement (Fig. 3a inset and
150 Supplementary Fig. 12). Single-layer 1T-TaSe₂/HOPG shows a similar dI/dV map with the
151 dominant LDOS intensity located near the outer rim of the stars-of-David at the lowest
152 conduction band peak (dI/dV maps at other energies also look similar, see Supplementary Fig. 10
153 and Supplementary Note 2).

154 The dI/dV map of single-layer 1T-TaSe₂/BLG obtained at a slightly higher bias of $V = 0.6$ V
155 (C_2) show LDOS that is related to the flower pattern in that it exhibits a nearly *inverse* flower
156 (i.e., dark areas at C_1 are bright at C_2 , see circled regions in Fig. 3e). At even higher energies the
157 single-layer 1T-TaSe₂ LDOS displays other intricate orbital textures. The map at 0.8 V (Fig. 3f),
158 for example, shows quasi-triangular patterns with intensity distributed near the outermost Ta C-
159 atoms (labeled according to the convention shown in Fig. 1d). This evolves into trimer-like

160 features at 1.1 V (Fig. 3g), and a network of “rings” with intensity near Ta B-atoms at $V = 1.2$ V
161 (Fig. 3h) (a complete set of constant-height dI/dV maps is shown in Supplementary Fig. 11).

162 To help quantify the complex energy-dependent LDOS distribution of single-layer 1T-TaSe₂,
163 we cross-correlated our dI/dV maps with a reference map taken at the maximum of the valence
164 band peak V_1 (Fig. 3c), which exhibits LDOS dominated by inner Ta A- and B-atoms. The
165 resulting cross-correlation values are color-coded in Fig. 3a and show that occupied states ($-1V <$
166 $V < 0$ V) all have a strong, positive cross-correlation (blue) with the valence band map at V_1 (i.e.,
167 the central Ta A- and B-atoms are bright at these energies and the C-atoms are darker). The
168 empty-state cross-correlation, however, is very different. At C_1 (where the flower pattern is
169 observed) the LDOS map is strongly anti-correlated (red) with the valence band map since the
170 LDOS here is dominated by Ta C-atoms. At slightly higher energy (C_2) the cross-correlation
171 flips to blue. This is due to the LDOS inversion that occurs at this energy (i.e., the inverse flower
172 pattern) which creates intensity at the interior A- and B-atoms. At higher energy the cross-
173 correlation flips again to red and stays red over a fairly wide energy range (~ 0.4 eV) before
174 flipping again to blue near C_3 .

175

176 **Energy gap reduction and quenching of unusual orbital texture in few-layer 1T-TaSe₂**

177 We examined the effect of interlayer coupling on 1T-TaSe₂ by studying the evolution in
178 electronic structure as 1T-TaSe₂ is stacked layer by layer. We first determined the star-of-David
179 CDW stacking order for bilayer and trilayer 1T-TaSe₂. As seen in the STM images of Fig. 1b
180 and Supplementary Fig. 1, the CDW stacking order follows the shifted triclinic structure
181 whereby inner Ta “A-atoms” sit on top of outer Ta “C-atoms”, similar to stacking observed in
182 bulk 1T-TaSe₂³². We observe that the energy gap for 1T-TaSe₂ narrows significantly when

183 interlayer coupling is added, as seen in the STM dI/dV spectra for bilayer and trilayer 1T-TaSe₂
184 shown in Fig. 4a. The bilayer energy gap reduces to 21 ± 8 meV while trilayer 1T-TaSe₂ shows a
185 reduction in LDOS at E_F that can be described as “semimetallic” but exhibits no true energy gap.

186 In addition to reducing the 1T-TaSe₂ energy gap, bilayer and trilayer formation also quench
187 the unusual orbital texture observed in the single-layer limit. As shown in the insets to Figs. 4b, c,
188 dI/dV maps of the lowest conduction band in bilayer and trilayer 1T-TaSe₂ show LDOS intensity
189 concentrated near the center of each star-of-David, in stark contrast to the flower-like orbital
190 texture observed in single-layer 1T-TaSe₂ at C_1 . This difference can also be seen in the color-
191 coded cross-correlation values of bilayer and trilayer 1T-TaSe₂ (Figs. 4b, c). Using the valence
192 band LDOS shown in the insets as a reference (which is similar to the single-layer valence band
193 LDOS of Fig. 3c), the bilayer and trilayer cross-correlation remain strongly positive (blue)
194 throughout the lowest conduction band (thus emphasizing that the LDOS here is concentrated on
195 the interior Ta A- and B-atoms). The distinctive flower pattern seen in single-layer 1T-TaSe₂ at
196 C_1 (Fig. 3d) is never seen in bilayer or trilayer LDOS at any bias (Supplementary Figs. 13, 14).

197 **Theoretical electronic structure of single-layer 1T-TaSe₂ via DFT+U simulations**

198 There are two main physical questions that we seek to answer regarding our measurements
199 of single- and few-layer 1T-TaSe₂. First, what type of insulator is single-layer 1T-TaSe₂? And,
200 second, what is the effect of interlayer coupling on 1T-TaSe₂ electronic behavior as new layers
201 are added? To address these questions we first performed a conventional band structure
202 calculation for freestanding single-layer 1T-TaSe₂ using density functional theory (DFT). From
203 an intuitive perspective, single-layer 1T-TaSe₂ is expected to have metallic band structure since
204 there are an odd number of Ta ions in the star-of-David unit cell (13) and each Ta⁴⁺ ion has only
205 one d -electron (in principle substrate charge transfer could alter the electron counting and/or the

206 CDW behavior³³, but in our case charge transfer effects from the graphene substrate are
207 negligible (Supplementary Fig. 15 and Supplementary Note 3)). As expected, the DFT band
208 structure of single-layer 1T-TaSe₂ in the CDW phase calculated using the PBE exchange
209 correlation functional shows a metallic half-filled band at E_F (Supplementary Fig. 16). This
210 theoretical result, however, strongly disagrees with our experimental data which shows
211 insulating behavior for single-layer 1T-TaSe₂ (Figs. 2, 3). An explanation for this significant
212 discrepancy is that since the metallic band is so narrow (only ~20 meV wide) it is unstable to
213 splitting into lower and upper Hubbard bands (LHB and UHB) due to a high on-site Coulomb
214 energy (U) (i.e., the condition that causes Mott insulators to arise from otherwise metallic
215 phases)¹.

216 To test for Mott insulator formation in single-layer 1T-TaSe₂ we modeled the effects of
217 electron correlation by performing DFT+U simulations. We find that the DFT+U band structure
218 for a ferromagnetic ground state with $U = 2$ eV reproduces most of our experimentally observed
219 electronic structure for single-layer 1T-TaSe₂ (the DFT+U results were sensitive to neither the
220 magnetic ground state nor the structural optimization conditions, and our U value is consistent
221 with previous simulations of related systems^{31,34,35} (see Supplementary Note 4 and
222 Supplementary Figs. 17-21)). The DFT+U band structure was first compared to our ARPES data
223 by unfolding it onto the Brillouin zone of an undistorted unit cell. As seen in Figs. 2c, d, and
224 Supplementary Fig. 22, it reproduces the gapped electronic structure and shows good overall
225 agreement with the ARPES spectra. In particular, DFT+U predicts that the LHB at -0.2 eV
226 originates mainly from Ta d_{z^2} orbitals, consistent with the higher ARPES intensity under p -
227 polarized light (Fig. 2a)³⁶.

228 The DFT+U simulations were also consistent with much of our STS data as shown in Fig. 5
229 which displays the simulated density-of-states spectrum and LDOS maps for single-layer 1T-
230 TaSe₂. The theoretical density-of-states spectrum (Fig. 5a (black line)) reproduces the dI/dV
231 spectrum (Fig. 3a) reasonably well in both the occupied and empty states. A LHB corresponding
232 to the experimental V_1 feature is seen, as well as an UHB corresponding to C_1 , along with higher
233 energy features that correspond to the experimental C_2 and C_3 features. The orbital texture
234 generated by the DFT+U calculations (Figs. 5b-h) also agree well with the experimental dI/dV
235 maps in the valence band and upper conduction band regimes (i.e., the energies corresponding to
236 filled states and levels above C_2).

237 However, there are significant discrepancies between the experimental and theoretical
238 LDOS maps in the low-energy conduction band region ($0 < E \lesssim 0.6$ eV) where the unusual
239 orbital texture is observed experimentally. This is most clearly seen by comparing the theoretical
240 UHB LDOS map at 0.2 eV (Fig. 5d) with the experimental dI/dV map at $V = 0.2$ V (Fig. 3d) (i.e.,
241 the energy corresponding to C_1). The calculated LDOS has high intensity in the central Ta A-
242 and B-atom regions (similar to what is seen in the LHB) while the experiment shows the flower
243 pattern (i.e., the experimental LDOS occupies the Ta C-atom region and is dark in the central
244 area). There also exists significant disagreement at the next higher energy band feature (C_2), as
245 seen by comparison of Figs. 3e and 5e. Here the theoretical orbital texture (Fig. 5e) shows
246 propeller-like structures with no central LDOS, while the experimental dI/dV map (Fig. 3e)
247 shows an inverse of the C_1 flower pattern which has LDOS in the interior region of the star-of-
248 David (a complete set of theoretical LDOS maps is shown in Supplementary Fig. 23).

249 **Unusual empty-state orbital texture at C_1 and C_2**

250 The good agreement between our DFT+U simulations and the majority of our ARPES
251 and STM/STS data provides strong evidence that single-layer 1T-TaSe₂ is a 2D Mott insulator.
252 However, the failure of the simulations to reproduce the unusual conduction band orbital texture
253 at C₁/C₂ implies that additional electron-electron interactions occur in single-layer 1T-TaSe₂ that
254 are not captured by DFT+U. Electrons injected from the STM tip into single-layer 1T-TaSe₂ at
255 the C₁/C₂ energies experience additional correlation effects originating from their Coulomb
256 interaction with electrons already present in the occupied electron states. Such behavior is
257 expected to arise due to the LHB charge distribution (Fig. 3c) which creates a spatially-varying
258 Coulomb repulsion landscape, $\tilde{U}(r)$, felt preferentially by electrons injected into UHB states
259 since they share a common orbital. $\tilde{U}(r)$ can be estimated by treating the LHB as a Gaussian
260 charge distribution within each star-of-David cluster and by calculating the resulting interaction
261 energy (Supplementary Note 5). This leads to a Coulomb landscape (Supplementary Fig. 24) that
262 is strongly repulsive to UHB electrons at the center of each star-of-David (where the LHB charge
263 density is large) and that has minima at precisely the locations of the six-fold C₁ flower petals
264 (where the LHB charge density is small). Given the composite nature of the UHB orbital (which
265 has contributions from 13 Ta atoms over the CDW cell) the unusual orbital texture at C₁/C₂ can
266 thus be understood as a redistribution of the UHB spectral density at the center of each star-of-
267 David up to higher energy in response to enhanced Coulomb interactions that arise from reduced
268 screening in 2D. The remaining state density of the composite UHB stays in the $\tilde{U}(r)$ minima
269 regions and gives rise to the peripheral six-fold C₁ flower petals. This picture is corroborated by
270 our observation that on the more strongly screened graphite substrate the LDOS distribution at
271 C₁ of single-layer 1T-TaSe₂ appears to be more smeared out around the outer rim of the star-of-
272 David cells, consistent with a less corrugated $\tilde{U}(r)$ landscape (Supplementary Fig. 10 and

273 Supplementary Note 2). Future theoretical treatments considering dynamical interactions could
274 potentially provide more insight into this unusual strong correlation phenomenon.

275 The effect of interlayer coupling on the shifted-stacked 1T-TaSe₂ electronic structure is to
276 weaken the Mott insulator phase, both in view of the observed energy gap reduction with
277 increased layer number as well as its effect on orbital texture. The bilayer and trilayer orbital
278 textures, for example, show no signs of the correlation-induced spectral density shift seen in the
279 single-layer material at C₁/C₂. Such weakening of the Mott behavior likely arises from an
280 increase in the effective inter-star-of-David hopping parameter (t) of the bilayer and trilayer due
281 to interlayer coupling, as well as a reduction in Coulomb interactions due to increased electronic
282 delocalization and screening.

283 **Outlook**

284 We have shown that single-layer 1T-TaSe₂ is a strongly correlated 2D Mott insulator
285 characterized by unusual orbital texture. Interlayer coupling weakens the Mott behavior,
286 consistent with the evolution of 1T-TaSe₂ into a metal as its thickness is increased layer-by-layer.
287 The Mott insulator phase seen in single-layer 1T-TaSe₂ thus offers a highly-tunable 2D platform
288 for future exploration of metal-insulator transitions¹ where the Coulomb interaction might be
289 further modified by substrate screening^{21,37}, the bandwidth by pressure³⁸, or the carrier density by
290 electrostatic gating^{6,8}.

291 **Acknowledgments**

292 We thank Patrick A. Lee and Dung-Hai Lee for helpful discussions. This research was
293 supported by the VdW Heterostructure program (KCWF16) (STS measurements and DFT
294 simulations) and the Advanced Light Source (sample growth and ARPES) funded by the

295 Director, Office of Science, Office of Basic Energy Sciences, Materials Sciences and
296 Engineering Division, of the US Department of Energy under Contract No. DE-AC02-
297 05CH11231. Support was also provided by National Science Foundation award EFMA-1542741
298 (surface treatment and topographic characterization), award DMR-1508412 (DFT+U and
299 theoretical STM/STS and ARPES analyses), award DMR-1507141 (electrostatic analysis), and
300 award EFRI-1433307 (CDW model development). The work at the Stanford Institute for
301 Materials and Energy Sciences and Stanford University (ARPES measurements) was supported
302 by the DOE Office of Basic Energy Sciences, Division of Material Science. Low-energy electron
303 diffraction measurements were supported by the National Natural Science Foundation of China
304 (grant no. 11227902). S. T. acknowledges the support by CPSF-CAS Joint Foundation for
305 Excellent Postdoctoral Fellows. H. R. acknowledges fellowship support from NRF, Korea
306 through Max Planck Korea/POSTECH Research Initiatives No. 2016K1A4A4A01922028. H.-
307 Z.T. acknowledges fellowship support from the Shenzhen Peacock Plan (Grant No. 827-000113,
308 KQJSCX20170727100802505, KQTD2016053112042971).

309 **Author contributions**

310 Y.C., W.R., and M.F.C. initiated and conceived the research. Y.C., W.R., H.-Z.T., R.L.,
311 S.K., F.L., and C.J. carried out STM/STS measurements and analyses. M.F.C supervised
312 STM/STS measurements and analyses. S.T., H.R., H.X., and T.J. performed sample growth and
313 ARPES measurements. S.-K.M., Z.-X.S., J.A.S., and Z.L. supervised sample growth and ARPES
314 measurements. M.W. performed DFT calculations and theoretical analyses. S.G.L. supervised
315 DFT calculations and theoretical analyses. J.E.M. performed electrostatic modeling. O.R.A. and
316 A.L. provided support for development of the CDW model. Y.C., W.R., and M.F.C. wrote the
317 manuscript with the help from all authors. All authors contributed to the scientific discussion.

318 **Competing interests**

319 The authors declare no competing interests.

320 **Data availability**

321 The data represented in Figs. 1f, 3a, 4, and 5a are available as source data in Supplementary
322 Data 1-4. All other data that support the plots within this paper and other findings of this study
323 are available from the corresponding author upon reasonable request.

324

325 **Code availability**

326 The codes used in this study are available from the corresponding author upon reasonable
327 request.

328

329 **Methods**

330 **Sample growth and ARPES measurements**

331 Single-layer 1T-TaSe₂ films were grown on epitaxial bilayer graphene terminated 6H-SiC(0001)
332 and cleaved HOPG substrates in a molecular beam epitaxy chamber operating at ultrahigh
333 vacuum (UHV, base pressure 2×10^{-10} Torr) at the HERS endstation of Beamline 10.0.1,
334 Advanced Light Source, Lawrence Berkeley National Laboratory. High purity Ta (99.9%) and
335 Se (99.999%) were evaporated from an electron-beam evaporator and a standard Knudsen cell,
336 respectively, with a Ta:Se flux ratio set between 1:10 and 1:20 and a substrate temperature of
337 660 °C. A higher substrate temperature (compared with our previous 1H-TaSe₂ growth at 550
338 °C²⁹) was used to facilitate the growth of the metastable 1T phase of TaSe₂. The growth process
339 was monitored by reflection high-energy electron diffraction. After growth, the films were

340 transferred *in-situ* into the analysis chamber (base pressure 3×10^{-11} Torr) for ARPES and core-
341 level spectra measurements. The ARPES system was equipped with a Scienta R4000 electron
342 analyzer. The photon energy was set at 51 eV (unless specified otherwise) with energy and
343 angular resolution of 12 meV and 0.1° , respectively. *p*- and *s*-polarized light were used, as
344 described elsewhere (ref. ³⁹). Before taking the films out of vacuum for STM/STS measurements,
345 Se capping layers with ~ 10 nm thickness were deposited onto the samples for protection. These
346 were later removed by UHV annealing at $\sim 200^\circ\text{C}$ for 3 hours.

347 **STM/STS measurements**

348 STM/STS measurements were performed using a commercial CreaTec STM/AFM system at $T =$
349 5 K under UHV conditions. To avoid tip artifacts, STM tips were calibrated on a Au(111)
350 surface by measuring its herringbone surface reconstruction and Shockley surface state before all
351 STM/STS measurements. Both W and Pt-Ir STM tips were used and yielded similar results. STS
352 dI/dV spectra were obtained using standard lock-in techniques with a small bias modulation at
353 401 Hz. The constant-height mode (i.e., feedback loop open) was used for collecting all dI/dV
354 conductance maps. Before obtaining each set of maps the STM tip was parked near the sample
355 surface for at least 8 hours to minimize piezoelectric drift effects.

356 **Electronic structure calculations**

357 First-principles calculations of single-layer 1T-TaSe₂ were performed using density functional
358 theory (DFT) as implemented in the Quantum ESPRESSO package⁴⁰. The onsite Hubbard
359 interaction was added through the simplified rotationally invariant approach using the same U
360 value for each Ta atom^{41,42}. A slab model with 16 Å vacuum layer was adopted to avoid
361 interactions between periodic images. We employed optimized norm-conserving Vanderbilt
362 pseudopotentials (ONCVSP) including Ta 5*s* and 5*p* semicore states (with a plane-wave energy

363 cutoff of 90 Ry)⁴³⁻⁴⁵ as well as the Perdew-Burke-Ernzerhof (PBE) exchange-correlation
364 functional⁴⁶ in the generalized gradient approximation (GGA). The structure was fully relaxed at
365 the DFT-PBE level until the force on each atom was less than 0.02 eV/Å (unless specified
366 otherwise). The resulting relaxed single-layer 1T-TaSe₂ in the $\sqrt{13} \times \sqrt{13}$ CDW phase has a
367 lattice constant of $a = 12.63$ Å. Spin-orbit coupling was not taken into account in our calculations
368 since it has a negligible influence on the band structure given the inversion symmetry of this
369 system. The unfolding of the band structure from the CDW supercell to the undistorted unit cell
370 was calculated using the BandUP code^{47,48} with band energies and wavefunctions obtained from
371 the Quantum ESPRESSO package.

372

373

374 **References:**

- 375
- 376 1 Imada, M., Fujimori, A. & Tokura, Y. Metal-insulator transitions. *Rev. Mod. Phys.* **70**,
377 1039-1263 (1998).
- 378 2 Keimer, B. & Moore, J. E. The physics of quantum materials. *Nat. Phys.* **13**, 1045-1055
379 (2017).
- 380 3 Kravchenko, S. *Strongly correlated electrons in two dimensions*. (Pan Stanford, 2017).
- 381 4 Dagotto, E. Correlated electrons in high-temperature superconductors. *Rev. Mod. Phys.*
382 **66**, 763-840 (1994).
- 383 5 Lee, P. A., Nagaosa, N. & Wen, X.-G. Doping a Mott insulator: Physics of high-
384 temperature superconductivity. *Rev. Mod. Phys.* **78**, 17-85 (2006).
- 385 6 Cao, Y. *et al.* Correlated insulator behaviour at half-filling in magic-angle graphene
386 superlattices. *Nature* **556**, 80-84 (2018).
- 387 7 Cao, Y. *et al.* Unconventional superconductivity in magic-angle graphene superlattices.
388 *Nature* **556**, 43-50 (2018).
- 389 8 Chen, G. *et al.* Evidence of a gate-tunable Mott insulator in a trilayer graphene moiré
390 superlattice. *Nat. Phys.* **15**, 237-241 (2019).
- 391 9 Chen, G. *et al.* Signatures of tunable superconductivity in a trilayer graphene moiré
392 superlattice. *Nature* **572**, 215-219 (2019).
- 393 10 Wilson, J. A. & Yoffe, A. D. The transition metal dichalcogenides discussion and
394 interpretation of the observed optical, electrical and structural properties. *Adv. Phys.* **18**,
395 193-335 (1969).
- 396 11 Fazekas, P. & Tosatti, E. Electrical, structural and magnetic properties of pure and doped
397 1T-TaS₂. *Philos. Mag. B* **39**, 229-244 (1979).
- 398 12 Perfetti, L. *et al.* Spectroscopic signatures of a bandwidth-controlled Mott transition at
399 the surface of 1T-TaSe₂. *Phys. Rev. Lett.* **90**, 166401 (2003).
- 400 13 Colonna, S. *et al.* Mott phase at the surface of 1T-TaSe₂ observed by scanning tunneling
401 microscopy. *Phys. Rev. Lett.* **94**, 036405 (2005).
- 402 14 Tosatti, E. & Fazekas, P. On the nature of the low-temperature phase of 1T-TaS₂. *J. Phys.*
403 *Colloq.* **37**, 165-168 (1976).
- 404 15 Sipos, B. *et al.* From Mott state to superconductivity in 1T-TaS₂. *Nat. Mater.* **7**, 960-965
405 (2008).
- 406 16 Ritschel, T. *et al.* Orbital textures and charge density waves in transition metal
407 dichalcogenides. *Nat. Phys.* **11**, 328-331 (2015).
- 408 17 Ma, L. *et al.* A metallic mosaic phase and the origin of Mott-insulating state in 1T-TaS₂.
409 *Nat. Commun.* **7**, 10956 (2016).
- 410 18 Cho, D. *et al.* Nanoscale manipulation of the Mott insulating state coupled to charge
411 order in 1T-TaS₂. *Nat. Commun.* **7**, 10453 (2016).
- 412 19 Ritschel, T., Berger, H. & Geck, J. Stacking-driven gap formation in layered 1T-TaS₂.
413 *Phys. Rev. B* **98**, 195134 (2018).
- 414 20 Lee, S.-H., Goh, J. S. & Cho, D. Origin of the Insulating Phase and First-Order Metal-
415 Insulator Transition in 1T-TaS₂. *Phys. Rev. Lett.* **122**, 106404 (2019).
- 416 21 Ugeda, M. M. *et al.* Giant bandgap renormalization and excitonic effects in a monolayer
417 transition metal dichalcogenide semiconductor. *Nat. Mater.* **13**, 1091-1095 (2014).
- 418 22 He, K. *et al.* Tightly Bound Excitons in Monolayer WSe₂. *Phys. Rev. Lett.* **113**, 026803
419 (2014).

420 23 Qiu, D. Y., da Jornada, F. H. & Louie, S. G. Screening and many-body effects in two-
421 dimensional crystals: Monolayer MoS₂. *Phys. Rev. B* **93**, 235435 (2016).

422 24 Halperin, B. I. & Rice, T. M. Possible Anomalies at a Semimetal-Semiconductor
423 Transition. *Rev. Mod. Phys.* **40**, 755-766 (1968).

424 25 Narozhny, B. N. & Levchenko, A. Coulomb drag. *Rev. Mod. Phys.* **88**, 025003 (2016).

425 26 Nakata, Y. *et al.* Monolayer 1T-NbSe₂ as a Mott insulator. *NPG Asia Materials* **8**, e321
426 (2016).

427 27 Nakata, Y. *et al.* Selective fabrication of Mott-insulating and metallic monolayer TaSe₂.
428 *ACS Appl. Nano Mater.* **1**, 1456-1460 (2018).

429 28 Di Salvo, F. J., Maines, R. G., Waszczak, J. V. & Schwall, R. E. Preparation and
430 properties of 1T-TaSe₂. *Solid State Commun.* **14**, 497-501 (1974).

431 29 Ryu, H. *et al.* Persistent charge-density-wave order in single-Layer TaSe₂. *Nano Letters*
432 **18**, 689-694 (2018).

433 30 Sohrt, C., Stange, A., Bauer, M. & Rosnagel, K. How fast can a Peierls-Mott insulator
434 be melted? *Faraday Discuss.* **171**, 243-257 (2014).

435 31 Qiao, S. *et al.* Mottness collapse in 1T-TaS_{2-x}Se_x transition-metal dichalcogenide: an
436 Interplay between localized and itinerant orbitals. *Phys. Rev. X* **7**, 041054 (2017).

437 32 Brouwer, R. & Jellinek, F. The low-temperature superstructures of 1T-TaSe₂ and 2H-
438 TaSe₂. *Physica B+C* **99**, 51-55 (1980).

439 33 Sanders, C. E. *et al.* Crystalline and electronic structure of single-layer TaS₂. *Phys. Rev.*
440 *B* **94**, 081404 (2016).

441 34 Darancet, P., Millis, A. J. & Marianetti, C. A. Three-dimensional metallic and two-
442 dimensional insulating behavior in octahedral tantalum dichalcogenides. *Phys. Rev. B* **90**,
443 045134 (2014).

444 35 Yu, X.-L. *et al.* Electronic correlation effects and orbital density wave in the layered
445 compound 1T-TaS₂. *Phys. Rev. B* **96**, 125138 (2017).

446 36 Moser, S. An experimentalist's guide to the matrix element in angle resolved
447 photoemission. *J. Electron Spectrosc.* **214**, 29-52 (2017).

448 37 Qiu, Z. *et al.* Giant gate-tunable bandgap renormalization and excitonic effects in a 2D
449 semiconductor. *Sci. Adv.* **5**, eaaw2347 (2019).

450 38 Yankowitz, M. *et al.* Dynamic band-structure tuning of graphene moiré superlattices with
451 pressure. *Nature* **557**, 404-408 (2018).

452 39 Tang, S. *et al.* Quantum spin Hall state in monolayer 1T'-WTe₂. *Nat. Phys.* **13**, 683-687
453 (2017).

454 40 Giannozzi, P. *et al.* QUANTUM ESPRESSO: a modular and open-source software
455 project for quantum simulations of materials. *J. Phys. Condens. Matter* **21**, 395502
456 (2009).

457 41 Liechtenstein, A. I., Anisimov, V. I. & Zaanen, J. Density-functional theory and strong
458 interactions: Orbital ordering in Mott-Hubbard insulators. *Phys. Rev. B* **52**, R5467-R5470
459 (1995).

460 42 Dudarev, S. L., Botton, G. A., Savrasov, S. Y., Humphreys, C. J. & Sutton, A. P.
461 Electron-energy-loss spectra and the structural stability of nickel oxide: An LSDA+U
462 study. *Phys. Rev. B* **57**, 1505-1509 (1998).

463 43 Hamann, D. R. Optimized norm-conserving Vanderbilt pseudopotentials. *Phys. Rev. B* **88**,
464 085117 (2013).

465 44 Schlipf, M. & Gygi, F. Optimization algorithm for the generation of ONCV
466 pseudopotentials. *Comput. Phys. Commun.* **196**, 36-44 (2015).
467 45 Scherpelz, P., Govoni, M., Hamada, I. & Galli, G. Implementation and Validation of
468 Fully Relativistic GW Calculations: Spin–Orbit Coupling in Molecules, Nanocrystals,
469 and Solids. *J. Chem. Theory Comput.* **12**, 3523-3544 (2016).
470 46 Perdew, J. P., Burke, K. & Ernzerhof, M. Generalized gradient approximation made
471 simple. *Phys. Rev. Lett.* **77**, 3865-3868 (1996).
472 47 Medeiros, P. V. C., Stafström, S. & Björk, J. Effects of extrinsic and intrinsic
473 perturbations on the electronic structure of graphene: Retaining an effective primitive cell
474 band structure by band unfolding. *Phys. Rev. B* **89**, 041407 (2014).
475 48 Medeiros, P. V. C., Tsirkin, S. S., Stafström, S. & Björk, J. Unfolding spinor wave
476 functions and expectation values of general operators: Introducing the unfolding-density
477 operator. *Phys. Rev. B* **91**, 041116 (2015).
478
479

480 **Fig. 1. Structure of single-layer 1T-TaSe₂ in the star-of-David CDW phase.** **a**, Top and side
481 view sketches of single-layer 1T-TaSe₂, including substrate. Clusters of 13 Ta atoms in star-of-
482 David CDW supercells are outlined, as well as the CDW unit cell. **b**, Large-scale STM
483 topograph of a typical 1T-TaSe₂ island shows monolayer and bilayer regions ($V_b = -0.5$ V, $I_t = 10$
484 pA, $T = 5$ K). **c**, A close-up STM image of single-layer 1T-TaSe₂. Each bright spot corresponds
485 to a star-of-David supercell ($V_b = -0.17$ V, $I_t = 3$ nA, $T = 5$ K). Black and orange parallelograms
486 mark CDW and atomic unit cells, respectively. **d**, Labels for Ta atoms in the star-of-David CDW
487 supercell depend on radial distance from center. **e**, Reflection high-energy electron diffraction
488 pattern of a submonolayer 1T-TaSe₂ film. **f**, X-ray photoelectron spectroscopy shows
489 characteristic peaks of Ta and Se core levels for a submonolayer 1T-TaSe₂ film.
490

491 **Fig. 2. ARPES and DFT+U band structure of single-layer 1T-TaSe₂.** ARPES spectra of
492 single-layer 1T-TaSe₂ acquired with **a**, *p*- and **b**, *s*-polarized light at $T = 12$ K along the Γ -K'
493 and Γ -M' directions defined in the undistorted (i.e., no CDW) unit cell Brillouin zone (yellow
494 hexagon in Fig. 2b inset). ARPES spectra have little intensity at low binding energies except for
495 coexisting 1H-TaSe₂ bands that cross E_F at $k \approx 0.5 \text{ \AA}^{-1}$ (white dashed lines). A strong flat band is
496 seen under *p*-polarized light in the first CDW Brillouin zone (black dashed box in **a**). The full
497 CDW Brillouin zone is sketched in the inset of **b** (black hexagon). **c**, DFT+U band structure ($U =$
498 2 eV) of single-layer 1T-TaSe₂ unfolded onto the undistorted unit cell Brillouin zone compared
499 to ARPES spectrum under *p*-polarized light (from **a**). **d**, Same DFT+U band structure as in **c**
500 compared to ARPES spectrum under *s*-polarized light (from **b**).

501

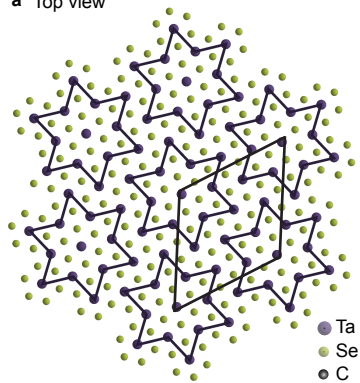
502

503 **Fig. 3. Experimental energy-resolved unusual orbital texture of single-layer 1T-TaSe₂.** **a**,
504 STS dI/dV spectrum of single-layer 1T-TaSe₂ shows a full energy gap bracketed by two STS
505 peaks labeled V_1 and C_1 ($f = 401$ Hz, $I_t = 50$ pA, $V_{\text{RMS}} = 20$ mV). Color shows cross-correlation
506 of dI/dV maps at different energies with the reference map shown in **c**. Inset shows how the
507 unusual orbital texture in **d** compares to atomic site locations (the 6-fold petal structure is shaded
508 gray in the inset). **b-h**, Constant-height dI/dV conductance maps of the same area for different
509 bias voltages show energy-dependent orbital texture ($f = 401$ Hz, $V_{\text{RMS}} = 20$ mV). The same star-
510 of-David CDW supercell is outlined in each map (orange line). Yellow dashed circles in **d**, **e**
511 highlight the unusual LDOS patterns at C_1 and C_2 and their relative spatial inversion.

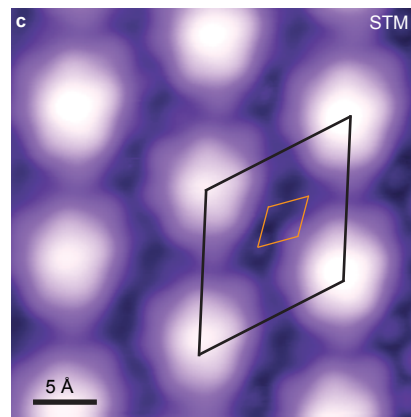
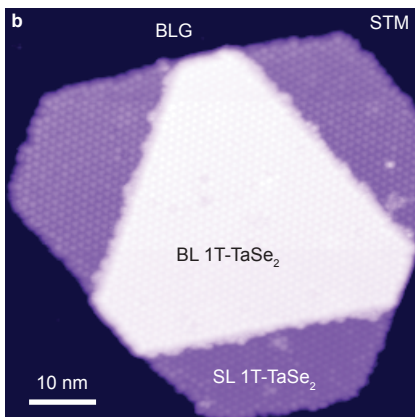
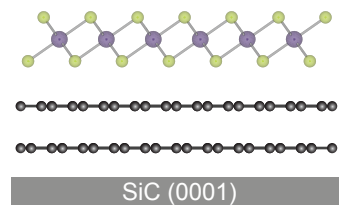
512
513 **Fig. 4. Energy gap reduction and quenching of unusual orbital texture in few-layer 1T-**
514 **TaSe₂.** **a**, STS dI/dV spectra for single-layer, bilayer, and trilayer 1T-TaSe₂ show how interlayer
515 coupling reduces the energy gap with an increasing number of layers. Spectra are shifted
516 vertically for viewing (horizontal dashed lines mark $dI/dV = 0$, $f = 401$ Hz, $V_{\text{RMS}} = 2$ mV). dI/dV
517 maps of the valence and conduction band LDOS as well as larger energy-scale dI/dV spectra of
518 **b**, bilayer, **c**, trilayer 1T-TaSe₂ ($f = 401$ Hz, $V_{\text{RMS}} = 20$ mV). Spatial cross-correlation values are
519 shown color-coded with references taken near the LDOS maximum of the valence band for
520 bilayer and trilayer 1T-TaSe₂. In contrast to single-layer 1T-TaSe₂, the lowest conduction band
521 for both bilayer or trilayer show no unusual orbital texture, thus resulting in positive cross-
522 correlation values (blue), indicating that LDOS is concentrated on the interior Ta A- and B-
523 atoms.
524

525
526 **Fig. 5. Theoretical orbital texture of single-layer 1T-TaSe₂ from DFT+U simulations. a,**
527 Theoretical density of states of single-layer 1T-TaSe₂ from DFT+U simulations ($U = 2$ eV).
528 Color shows cross-correlation of LDOS maps at different energies with respect to the reference
529 map in **c** (-0.2 eV). **b-h**, Theoretical LDOS maps of single-layer 1T-TaSe₂ from DFT+U
530 simulations ($U = 2$ eV). The same star-of-David supercell is outlined in each map (orange line).
531 Yellow dashed circles in **d**, **e** highlight two star-of-David clusters which show very different
532 theoretical conduction band orbital texture compared to experimental C_1 and C_2 features in Figs.
533 3d, e.

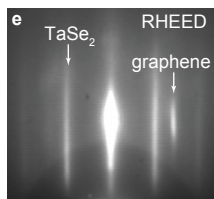
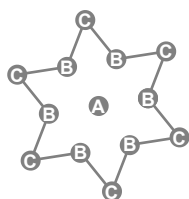
a Top view



Side view



d



f

